Article

https://doi.org/10.5194/gchron-6-541-2024

Short communication/technical note
18 Oct 2024

Technical note: Altitude scaling of ^{36}Cl production from Fe

Angus K. Moore and Darryl E. Granger

Abstract

Cosmogenic nuclide production rates depend on the excitation functions of the underlying nuclear reactions and the intensity and energy spectrum of the cosmic-ray flux. The cosmic-ray energy spectrum shifts towards lower average energies with decreasing altitude (increasing atmospheric depth), so production rate scaling will differ for production reactions that have different energy sensitivities. Here, we assess the possibility of the unique scaling of ^{36}Cl production from Fe by modeling changes in the $^{36}Cl_{Fe}/^{36}Cl_K$ and $^{36}Cl_{Fe}/^{10}Be_{qtz}$ production ratios with altitude. We evaluate model predictions against measured ^{36}Cl concentrations in magnetite and K-feldspar and ^{10}Be concentrations in quartz from granitic rocks exposed across an elevation transect (ca. 1700–4300 m a.s.l.) in western North America. The data are broadly consistent with model predictions. The null hypothesis that $^{36}Cl_{Fe}/^{10}Be_{qtz}$ and $^{36}Cl_{Fe}/^{36}Cl_K$ production ratios are invariant with altitude can be rejected at the 90 % confidence level. Thus, reaction-specific scaling factors will likely yield more accurate results than non-reaction-specific scaling factors when scaling ^{36}Cl production in Fe-rich rocks and minerals.

How to cite. Moore, A. K. and Granger, D. E.: Technical note: Altitude scaling of ^{36}Cl production from Fe, Geochronology, 6, 541–552, https://doi.org/10.5194/gchron-6-541-2024, 2024.

Received: 03 Apr 2024 – Discussion started: 15 Apr 2024 – Revised: 17 Aug 2024 – Accepted: 25 Aug 2024 – Published: 18 Oct 2024

1 Introduction

Cosmogenic nuclides are produced in rock exposed at the surface of the Earth through nuclear reactions between cosmic rays and target nuclei in the rock. These cosmogenic nuclides produced in situ give rise to a family of geochronologic systems that can be used to determine surface exposure ages, erosion rates, and burial dates of late Cenozoic sediments (von Blanckenburg and Willenbring, 2014; Granger et al., 2013). General application of cosmogenic nuclide geochronology across the surface of the Earth requires modeling how cosmogenic nuclide production rates scale in space and time due to the geomagnetic modulation of the primary cosmic-ray flux and the attenuation of cosmic radiation in the atmosphere.

The most important cosmogenic nuclide production reactions are high-energy nucleon (neutron and proton) spallation. The production rate of a cosmogenic nuclide by spallation at any location on Earth's surface depends on the excitation functions of the underlying nuclear reactions (i.e., the cross section, a measure of reaction probability, as a function of incident particle energy) and the intensity and energy distribution of the cosmic radiation at that location. Monte Carlo simulations of the atmospheric nucleonic cascade show that nucleon energy spectra shift towards lower average energies with decreasing elevation (Argento et al., 2015a,b, 2013). This implies that the production ratio between two reactions with different energy sensitivities changes with altitude.

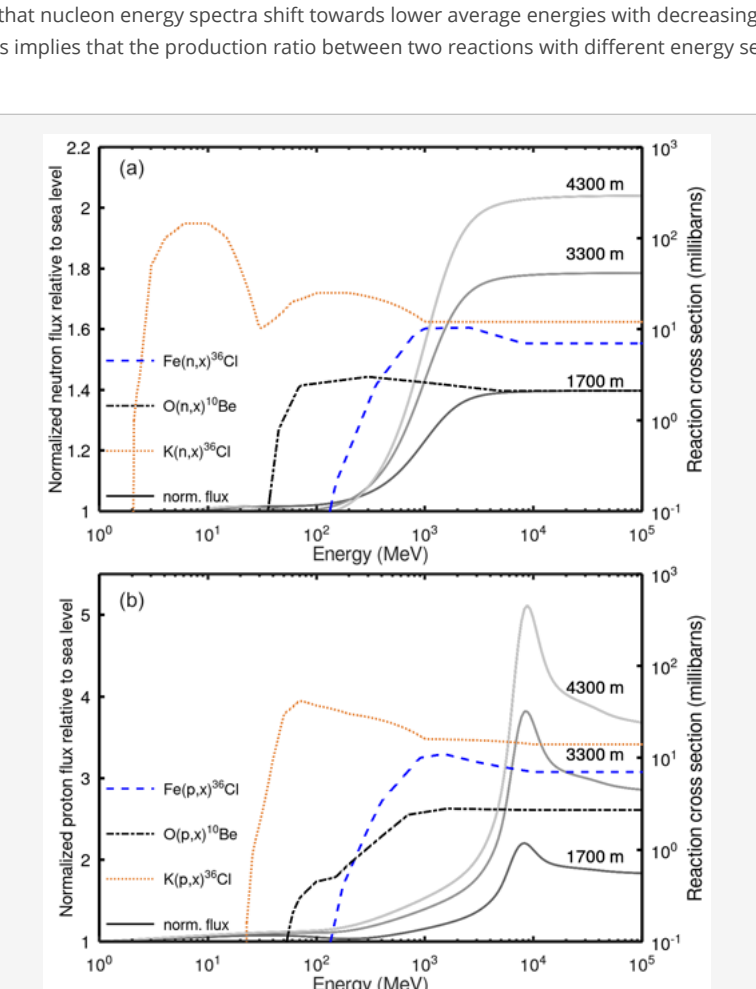

Figure 1 Comparison of high-energy particle flux energy spectra (grey curves; left y axis) with excitation functions (dashed curves; right y axis). **(a)** Neutron energy spectra at 1700, 3300, and 4300 m a.s.l. (corresponding to the elevations of the calibration sites) at a cutoff rigidity of 6.3 GV and a long-term solar modulation constant of 462 MV (the approximate average at the calibration sites since 21 ka, the Last Glacial Maximum) normalized by the flux at 1 MeV to account for increased neutron fluxes with altitude and by the spectrum at sea level to highlight changes in the energy spectrum with altitude (left y axis) and excitation functions for spallation production of ^{36}Cl from Fe and K and ^{10}Be from O (Reedy et al., 2013) (right y axis). **(b)** Equivalent normalized proton energy spectra and excitation functions.

Download

Several studies have investigated changing production ratios with altitude. For example, the ^{3}He/^{10}Be ratio has been observed to increase with altitude in the Himalaya (Amidon et al., 2008; Gayer et al., 2004), although a similar signal is ambiguously absent in datasets from the Andes and Mount Kilimanjaro (Blard et al., 2013; Schimmelpfennig et al., 2011). Likewise, Corbett et al. (2017) measured an ^{26}Al/^{10}Be ratio in quartz at sea level and high latitude (SLHL) that is approximately 7 % higher than the conventional ratio of ca. 6.8 originally calibrated at high elevation and mid-latitude (Nishiizumi et al., 1989). Global analysis of the ^{26}Al/^{10}Be ratio data in quartz also supports spatial variation in this production ratio (Halsted et al., 2021). However, because the reactions producing ^{10}Be and ^{26}Al in quartz are sensitive to the lower end of the high-energy spectrum, the signal is subtle and may be easily overprinted by, for example, inherited muon-produced nuclides.

Changes in the production ratio with altitude should be most clearly resolvable between two reactions that are widely separated in energy sensitivity. Cosmogenic production rates fall steeply below ca. 500 MeV, the maximum energy associated with secondary recoil nucleons, experience little change with elevation because the slowing down of secondary nucleons from this energy to rest occurs essentially locally in the atmosphere (Lal and Peters, 1967). This means that all reactions sensitive primarily to energies below 500 MeV should exhibit only modest differences in scaling with altitude, regardless of the shape of the underlying excitation functions, whereas reactions that peak above 500 MeV should be more rapidly attenuated in the atmosphere.

Of the commonly measured in-situ-produced cosmogenic nuclides, ^{36}Cl offers the widest range of practical production pathways, including spallation from four major rock-forming elements (K, Ca, Ti, and Fe). These reactions encompass a wide range of energy sensitivities and can be isolated by analyzing mineral separates with tightly defined target chemistries. Of the four reactions, spallation from Fe has the highest threshold and peak (Schiekel et al., 1996; Reedy, 2013) (Fig. 1) and thus is most likely to exhibit a clearly detectable departure from the other ^{36}Cl production pathways. Previous work studied the ^{36}Cl production rate from Fe in magnetite relative to ^{10}Be in quartz (Moore and Granger, 2019a), although it did not conclusively confirm or refute reaction-specific scaling. In that study, the difference in the time-integrated geomagnetic cutoff rigidity between widely separated calibration sites may have offset the effect of a ca. 1800 m elevation difference.

Here, we directly evaluate reaction-specific scaling of ^{36}Cl production from Fe by examining changes in $^{36}Cl_{Fe}/^{36}Cl_K$ and $^{36}Cl_{Fe}/^{10}Be_{qtz}$ production ratios with altitude. First, ratios are modeled as a function of altitude using cosmic-ray energy spectra in conjunction with available excitation functions. Model predictions are then tested against data from Moore and Granger (2019a) and new measurements of ^{36}Cl in magnetite and K-feldspar and ^{10}Be in quartz from granitic boulders exposed at elevations of ca. 1700 and 4300 m a.s.l., but with similar time-integrated cutoff rigidities, in western North America. The results have implications for accurately estimating ^{36}Cl production rates in Fe-rich rocks (e.g., peridotite or basalt) and mineral separates (e.g., magnetite), which are increasingly used to determine erosion rates and exposure ages in quartz-poor mafic and ultramafic landscapes (e.g., Leontaritis et al., 2022; Moore et al., 2024; Moore and Granger, 2019b).

2 Methods

2.1 Production model

To predict the scaling behavior of ^{36}Cl production from Fe, we model production rate changes across an altitude transect. Production rates are calculated by integrating the product of the reaction cross section and particle flux across all cosmic-ray energies as follows (Lal and Peters, 1967):

$$P_i = \sum_j N_j \sum_k \int_0^\infty \frac{d\Phi_k(E_k)}{dE_k} \sigma_{ijk}(E_k) dE_k, \quad (1)$$

where P_i is the production rate of nuclide i (in atoms g^{-1} yr^{-1}), N_j is the number of target nuclei j per gram of target material, $\sigma_{ijk}(E_k)$ is the cross section for production of nuclide i on target atom j by particle k at energy level E_k, and $\Phi_k(E_k)$ is the omnidirectional flux of particles of type k of energy E that are incident at the location of interest (i.e., $d\Phi_k(E_k)/dE_k$ is the differential energy spectrum). Cross sections are typically derived from irradiation experiments (e.g., Schiekel et al., 1996), whereas particle fluxes are usually estimated from Monte Carlo modeling of the cosmic-ray cascade (e.g., Masarik and Beer, 2009).

Direct calculation of cosmogenic nuclide production rates using Eq. (1) has historically been impeded, in part, by the high computational costs of Monte Carlo modeling of the evolution of the cosmic-ray cascade through the atmosphere. The PARMA model (Sato et al., 2008), which drives the widely applied Lifton–Sato–Dunai scaling model for in situ production rates (Lifton et al., 2014), provides a computationally efficient way of estimating cosmic-ray intensities and energy spectra using analytical functions fit to the output of Monte Carlo simulations. Precision in the nucleon spectrum from PARMA is similar to that derived directly from Monte Carlo models (Sato et al., 2008). Statistical uncertainties in predicted nucleon fluxes tend to increase towards sea level, where they are estimated at 20 %; however, the model fits available intensity observations with significantly better fidelity (Lifton et al., 2014), especially for the higher-energy nucleonic component of the cascade. We use the PARMA model, as implemented in Lifton et al. (2014), to model $\Phi_k(E_k)$. Figure 1 illustrates the modeled increase in the intensity of the high-energy portion of the cosmic-ray nucleon spectrum with increasing in altitude.

Excitation functions are taken from the compilation of Reedy (2013) and consist of evaluated cross sections compiled chiefly from the CSISRS (Cross Section Information Storage and Retrieval System) database maintained by Brookhaven National Laboratory. The excitation function for ^{36}Cl production from Fe by protons as measured by Schiekel et al. (1996). The estimate of the excitation function for the corresponding neutron reaction is broadly similar, with a slightly lower threshold (Fig. 1). This is consistent with the tendency of neutron and proton cross sections to be comparable at high energies. Furthermore, ^{36}Cl is intermediate in mass between two stable isotopes, ^{35}Cl and ^{37}Cl. Neutron and proton reactions that make a nuclide between two stable nuclides often have similar excitation functions (Reedy, 2013).

Table 1 Sample locations and characteristics.

ID	Latitude (dec. deg.)	Longitude (dec. deg.)	Elevation (m a.s.l.)	Thickness[a] (cm)	Feature	Exposure model
Owens Valley						
OV19-1	37.416	−118.630	1702	12	Moraine	Constant exposure
OV19-2	37.416	−118.630	1701	12	Moraine	Constant exposure
OV19-3	37.416	−118.630	1701	10	Moraine	Constant exposure
Sierra Nevada						
BL15-1	37.166	−118.618	3365	3	Erratic	Constant exposure
BL15-2	37.167	−118.619	3363	4	Erratic	Constant exposure
BL15-3	37.167	−118.622	3360	4	Erratic	Constant exposure
LL15-1	37.392	−118.766	3328	6	Erratic	Constant exposure
LL15-2	37.403	−118.756	3318	4	Erratic	Constant exposure
Mount Evans						
97EV14B	39.588	−105.644	4267	25	Blockfield	Steady-state erosion

[a] All samples are granitic in composition, with an assumed density of 2.7 g cm^{-3}.

Download Print Version | Download XLSX

2.2 Calibration samples

We examine production ratios across three sites that span a ca. 2600 m elevation transect at mid-latitude in western North America (Fig. 2; Table 1). Three samples were collected at the low-elevation site, which is a moraine located at the mouth of Pine Creek Canyon in Owens Valley, California, at ca. 1700 m a.s.l. This moraine corresponds to the Tioga 2 stage of glaciation in the Sierra Nevada between ca. 25–20 ka (Phillips et al., 2009). The mid-elevation samples (collected from two sites at approximately 3300 m a.s.l.) were previously described in Moore and Granger (2019a). These samples were collected from the surfaces of erratic boulders located behind the late-glacial Recess Peak (13.3 ka) and Tioga 4 (15.8 ka) moraines in the Sierra Nevada of California (Phillips, 2016). A legacy sample, collected in 1997 by David Elmore from ca. 4300 m a.s.l. on Mount Evans in Colorado, forms the uppermost member of the transect. This sample was situated near the Mount Evans summit parking lot in an unglaciated alpine blockfield that we model as eroding in steady state. The sample consists of a whole boulder that was crushed in 1997. No record survives of the initial geometry of the boulder. Therefore, we estimate the sample thickness from the total sample mass, approximating the boulder geometry as a cube (Table 1). The uncertainty introduced by this approach is unlikely to significantly affect the results of the analysis because production ratios are sensitive to sample thickness only insofar as different production mechanisms have different attenuation lengths or radioactive decay is significant. For Owens Valley and Mount Evans, magnetite, K-feldspar, and quartz separates were analyzed, whereas only magnetite and quartz were examined at the mid-elevation Sierra Nevada sites.

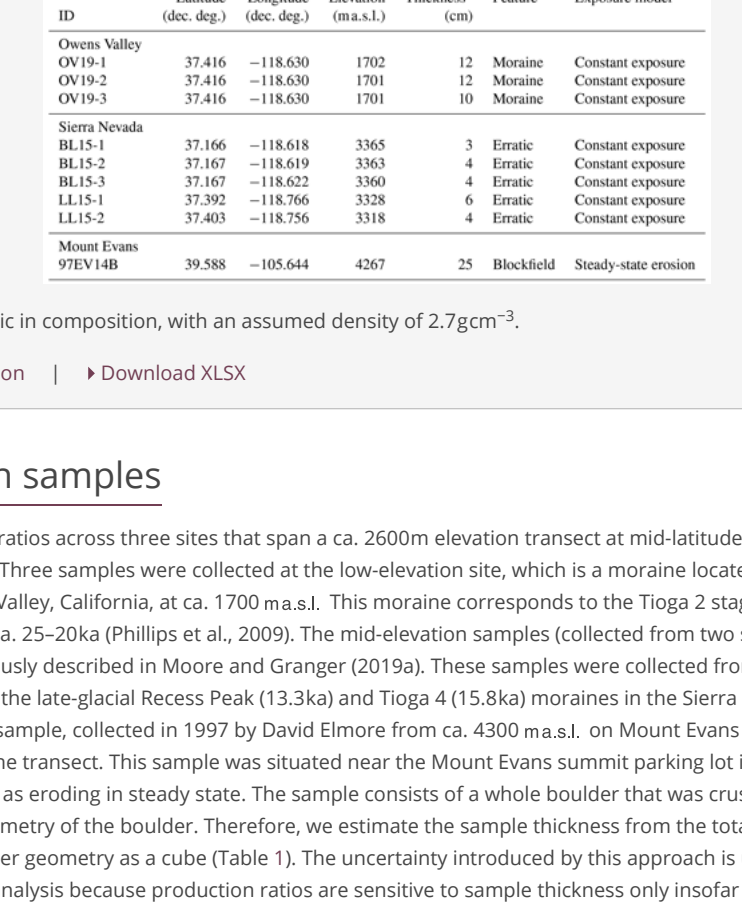

Figure 2 Location of the calibration sites within western North America (purple diamonds). The sites are located between 38–40° N, minimizing the inter-site variability in cutoff rigidity.

2.3 Analytical methods

The calibration samples were crushed, and magnetite and K-feldspar were separated and prepared for ^{36}Cl measurement. Magnetite was isolated from the crushed rock using repeated cycles of magnetic separation with rare-earth magnets and grinding with zirconia balls on a wrist-action shaker. Separates were leached once in dithionite–citrate–bicarbonate to remove secondary Fe-oxide minerals and then in 10 % nitric acid, followed by 1 % $NH_4(OH)$, to remove any adsorbed chloride. Clean magnetite was spiked with a ^{35}Cl-enriched carrier ($^{35}Cl/^{37}Cl$ = 273) and dissolved in high-purity oxalic acid. After dissolution, precipitates were removed by centrifugation. Next, Cl was precipitated from solution as AgCl by adding HNO_3 and an excess of $AgNO_3$. Feldspar separates were obtained from the 250–500 µm fraction of the crushed sample through froth flotation and density separation in lithium heteropolytungstate. Feldspar grain surfaces were cleaned in 10 % HNO_3. The samples were then spiked and dissolved in a solution of ca. 30 % HF and 1 % HNO_3. After dissolution, the solutions were refrigerated to 2 °C to promote formation of fluoride precipitates, which were removed by centrifugation to reduce solution viscosity. Chloride was then precipitated from the solution as AgCl. The AgCl precipitates from both the magnetite and feldspar samples were dissolved in $NH_4(OH)$ and purified of SO_4^{2-} through precipitation with Ba^{2+} and anion chromatography. The final AgCl product was dried and loaded into AgBr-filled copper cathodes for the measurement of $^{36}Cl/Cl$ and $^{35}Cl/^{37}Cl$ by accelerator mass spectrometry (AMS) at PRIME Lab, Purdue University. Measurements were normalized to the Sharma et al. (1990) standard, using the dilution with a $^{36}Cl/Cl$ ratio of 1600×10^{-15}.

Sample target and bulk-rock chemistries, necessary for modeling ^{36}Cl production, were determined by inductively coupled plasma–optical emission spectrometry (ICP–OES), using a Horiba Ultima Expert™ spectrometer. Aliquots of sample material were taken for target chemistry measurements immediately prior to dissolution. Approximately 50 mg was dissolved in concentrated HF and then evaporated to dryness, redissolved in HNO_3, and again evaporated to dryness before being taken up in 5 % HNO_3 for measurement. Stable Cl concentrations were determined from the isotope dilution of the ^{35}Cl-enriched carrier. For the measurement of trace elements important for controlling low-energy neutron fluxes in the subsurface (i.e., B, Sm, U, Th, Gd, Cr, and Li), ca. 20 g of rock was powdered in a ring-and-puck mill and ca. 250 mg of homogenized powder dissolved in HF and prepared for measurement in the same way as the target fraction. However, this approach cannot be used to determine Si, which forms a volatile fluoride. To determine Si and other major element concentrations, ca. 100 mg of rock powder was fused in a 50:50 mixture of lithium metaborate and lithium tetraborate at 1000 °C for 30 min. The fusion cake was dissolved in 50 % HNO_3 and diluted to 5 % HNO_3 for measurement. Analytical water was approximated from the loss on ignition (LOI) at 1000 °C, assuming all evolved volatiles represent H_2O.

Quartz separates were obtained from the 250–500 µm fraction of the crushed samples, using froth flotation and leaching in 1 % HF/HNO_3. The quartz separates were spiked with an in-house ^{9}Be carrier and dissolved in concentrated HF. After dissolution, 1 mL H_2SO_4 was added to maintain the volume, and then the HF was evaporated. Beryllium was isolated from the H_2SO_4, using a rapid separation scheme. First, amphoteric species were partitioned into the supernatant by precipitation of other species at pH 14. Beryllium was then precipitated from the supernatant by adjusting to pH 9 with HCl, which coprecipitates some Al and Fe. The precipitates were dissolved in 0.4 M oxalic acid, and negatively charged oxalate complexes of Al and Fe were separated from the neutral $Be(C_2O_4)^0$ complex by passing the solution through an anion exchange column (Dowex 1×8 100–200 mesh). Beryllium was precipitated directly from the oxalic acid solution with $NH_4(OH)$ and polished by reprecipitating twice. The $Be(OH)_2$ product was calcined under an acetylene flame, mixed with a Nb binder, and loaded into a stainless-steel cathode for $^{10}Be/^{9}Be$ measurement by AMS. Measurements were normalized to the standard described by Nishiizumi et al. (2007), with a nominal $^{10}Be/^{9}Be$ ratio of 2.851×10^{-12}.

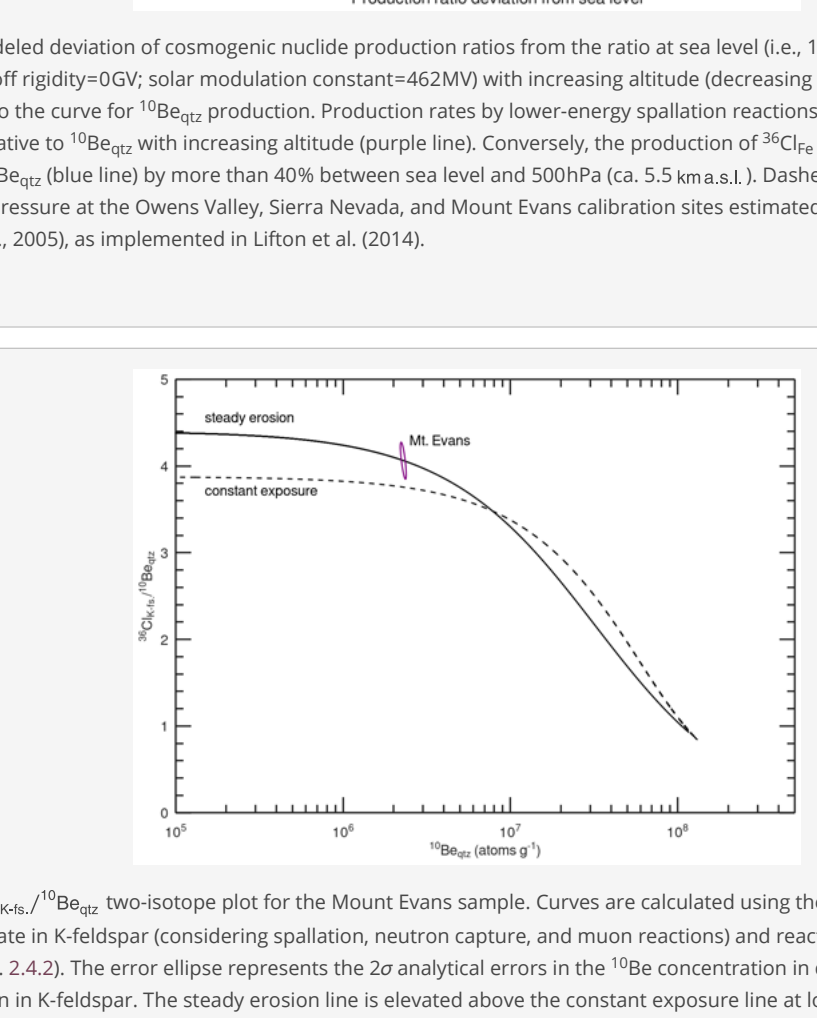

Figure 3 Modeled deviation of cosmogenic nuclide production ratios from the ratio at sea level (i.e., 1013.25 hPa) at high latitude (cutoff rigidity = 0 GV; solar modulation constant = 462 MV) with increasing altitude (decreasing pressure). Curves are normalized to the curve for $^{10}Be_{qtz}$ production. Production rates by lower-energy spallation reactions (e.g., $^{36}Cl_K$) decrease modestly relative to $^{10}Be_{qtz}$ with increasing altitude (purple line). Conversely, the production of $^{36}Cl_{Fe}$ increases with altitude relative to $^{10}Be_{qtz}$ (blue line) by more than 40 % between sea level and 500 hPa (ca. 5.5 km a.s.l.). Dashed horizontal lines indicate air pressure at the Owens Valley, Sierra Nevada, and Mount Evans calibration sites estimated from the ERA40 model (Uppala et al., 2005), as implemented in Lifton et al. (2014).

Download

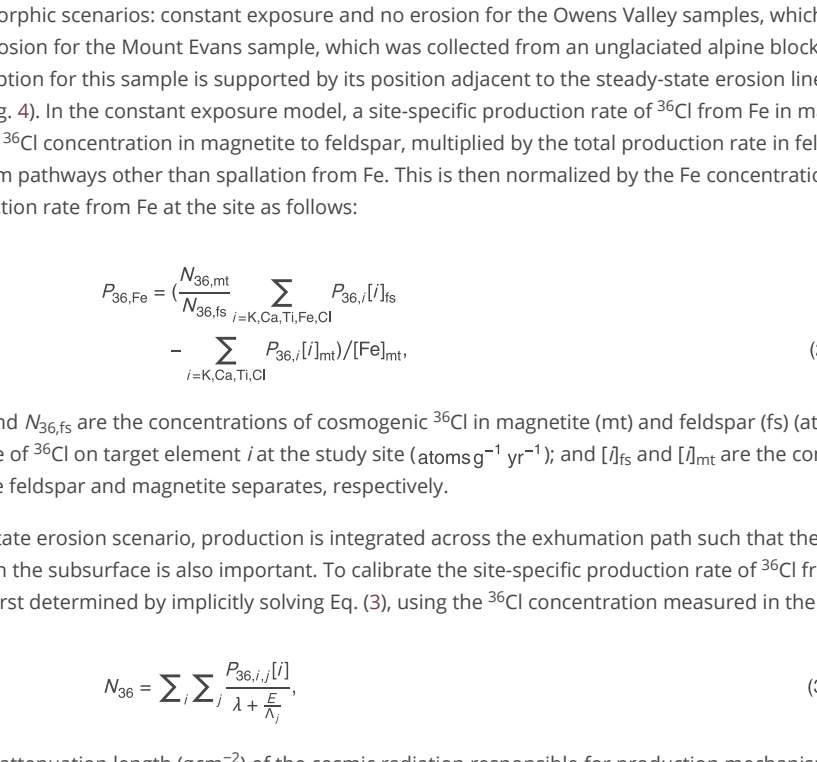

Figure 4 $^{36}Cl_{K\text{-fs.}}/^{10}Be_{qtz}$ two-isotope plot for the Mount Evans sample. Curves are calculated using the sample-specific ^{36}Cl production rate in K-feldspar (considering spallation, neutron capture, and muon reactions) and reaction-specific attenuation lengths (Sect. 2.4.2). The error ellipse represents the 2σ analytical errors in the ^{10}Be concentration in quartz and ^{36}Cl concentration in K-feldspar. The steady erosion line is elevated above the constant exposure line at low ^{10}Be concentration (i.e., short exposure ages or fast erosion rates) because of the greater subsurface attenuation length of ^{36}Cl production from K. The Mount Evans sample overlaps with the steady erosion line at 1σ and is greater than 2σ from the constant exposure line, indicating that steady-state erosion is a more plausible geomorphic model than constant exposure.

Download

2.4 Calculations

2.4.1 Production rate calibration

Production rates of ^{36}Cl from Fe are calibrated against ^{36}Cl in K-feldspar and ^{10}Be in quartz. The calibrations assume two end-member geomorphic scenarios: constant exposure and no erosion for the Owens Valley samples, which are moraine clasts, and steady-state erosion for the Mount Evans sample, which was collected from an unglaciated alpine blockfield. The steady-state erosion assumption for this sample is supported by its position adjacent to the steady-state erosion line on a $^{36}Cl/^{10}Be$ two-isotope plot (Fig. 4). In the constant exposure model, a site-specific production rate of ^{36}Cl from Fe in magnetite is calculated from the ratio of the ^{36}Cl concentration in magnetite to feldspar, multiplied by the total production rate in feldspar and minus the production from pathways other than spallation from Fe. This is then normalized by the Fe concentration in magnetite to derive the ^{36}Cl production rate from Fe at the site as follows:

$$P_{36,Fe} = \Big(\frac{N_{36,mt}}{N_{36,fs}} \sum_{i=K,Ca,Ti,Fe,Cl} P_{36,i}[i]_{fs} - \sum_{i=K,Ca,Ti,Cl} P_{36,i}[i]_{mt}\Big)/[Fe]_{mt}, \quad (2)$$

where $N_{36,mt}$ and $N_{36,fs}$ are the concentrations of cosmogenic ^{36}Cl in magnetite (mt) and feldspar (fs) (atoms g^{-1}); $P_{36,i}$ is the production rate of ^{36}Cl on target element i at the study site (atoms g^{-1} yr^{-1}); and $[i]_{fs}$ and $[i]_{mt}$ are the concentrations of target element i in the feldspar and magnetite separates, respectively.

In the steady-state erosion scenario, production is integrated across the exhumation path such that the attenuation length scale of each reaction in the subsurface is also important. To calibrate the site-specific production rate of ^{36}Cl from Fe, the erosion rate (E) (g cm^{-2} yr^{-1}) is first determined by implicitly solving Eq. (3), using the ^{36}Cl concentration measured in the feldspar:

$$N_{36} = \sum_i \sum_j \frac{P_{36,i,j}[i]}{\lambda + \frac{E}{\Lambda_j}}, \quad (3)$$

where Λ_j is the attenuation length (g cm^{-2}) of the cosmic radiation responsible for production mechanism j, λ is the decay constant of ^{36}Cl (yr^{-1}), and N_{36} is the concentration of ^{36}Cl (atoms g^{-1}). The erosion rate is then used in conjunction with $N_{36,mt}$ and production rates from pathways other than spallation on Fe to again solve Eq. (3) but this time for the site-specific production rate of ^{36}Cl from Fe. Importantly, Eq. (3) gives more weight to production from muon interactions than Eq. (2) because of the longer muon than nucleon attenuation length in the subsurface.

Table 2 Calibrated (Cal.) ^{36}Cl production rates from Fe and $^{36}Cl_{Fe}/^{36}Cl_K$ and $^{36}Cl_{Fe}/^{10}Be_{qtz}$ scaling factor ratios. K-fs. stands for K-feldspar.

ID	Production rate from Fe at site: Cal. vs. K-fs. (atoms g Fe^{-1} yr^{-1})	Production rate from Fe at site: Cal. vs. quartz (atoms g Fe^{-1} yr^{-1})	Production rate from Fe at SLHL: Cal. vs. K-fs. (atoms g Fe^{-1} yr^{-1})	Production rate from Fe at SLHL: Cal. vs. quartz (atoms g Fe^{-1} yr^{-1})	Scaling factor ratio: Norm. to $^{36}Cl_K$	Scaling factor ratio: Norm. to $^{10}Be_{qtz}$
New data (this study)						
OV19-1	2.19 ± 0.45	2.30 ± 0.47	0.54 ± 0.11	0.57 ± 0.12	0.47 ± 0.10*	0.47 ± 0.10
OV19-2	5.21 ± 0.37	5.34 ± 0.37	1.29 ± 0.09	1.32 ± 0.09	1.11 ± 0.08	1.10 ± 0.08
OV19-3	5.43 ± 0.38	5.59 ± 0.36	1.34 ± 0.09	1.38 ± 0.09	1.15 ± 0.08	1.14 ± 0.07
97EV14B	36.9 ± 2.6	36.8 ± 2.5	1.31 ± 0.09	1.31 ± 0.09	1.38 ± 0.10	1.29 ± 0.09
Old data (Moore and Granger, 2019a)						
BL15-1	–	19.3 ± 1.4	–	1.43 ± 0.10	–	1.32 ± 0.09
BL15-2	–	18.1 ± 1.4	–	1.34 ± 0.10	–	1.24 ± 0.09
BL15-3	–	16.8 ± 1.3	–	1.25 ± 0.10	–	1.15 ± 0.09
LL15-1	–	16.6 ± 1.1	–	1.25 ± 0.08	–	1.15 ± 0.08
LL15-2	–	17.3 ± 1.4	–	1.31 ± 0.10	–	1.20 ± 0.10

* OV19-1 is omitted from the analysis as an outlier (see Sect. 3.2).

Download Print Version | Download XLSX

Production of ^{36}Cl from Fe is also calibrated relative to ^{10}Be in quartz, which requires a formulation that accounts for the differential decay between ^{10}Be and ^{36}Cl. Here, the approaches discussed in Moore and Granger (2019a) for the constant exposure and steady-state erosion cases are used. Calibrated production rates are then corrected for ^{36}Cl production pathways in magnetite other than spallation from Fe and normalized by the Fe concentration in the same manner as in Eq. (2). For the mid-elevation Sierra Nevada sites, the production rates calibrated in Moore and Granger (2019a) are adopted without modification (Table 2).

Reference spallation production rates at SLHL are taken from Marrero et al. (2016) and are scaled to the study sites using reaction-specific scaling factors from the Lifton–Sato–Dunai model (Lifton et al., 2014). Muon production of ^{36}Cl and ^{10}Be is modeled with depth in the subsurface, following Marrero et al. (2016), and parameterized by fitting coefficients and attenuation lengths for two exponential terms to the slow-negative-muon depth profile and a single exponential term to the fast-muon-depth profile. This approach captures the altitude dependence of muon attenuation lengths (Balco, 2017).

2.4.2 Reaction-specific spallation attenuation lengths

Spallation reactions that display different attenuation behavior in the atmosphere likely also differ in the subsurface. Capturing this effect is important for accurately calibrating production rates using samples from eroding surfaces. The higher average atomic mass of nuclei in the subsurface than the atmosphere leads to a higher nucleon multiplicity (i.e., the average number of nucleons ejected from a target nucleus during a cosmic-ray reaction). Reactions that are sensitive to the energies of tertiary nucleons, such as production of ^{36}Cl from K, which has a threshold of about 1 MeV, should therefore attenuate more slowly in the subsurface than other reactions (Argento et al., 2015b).

This effect was explored using Monte Carlo modeling by Argento et al. (2015b), who presented polynomial functions describing production of ^{36}Cl from K with depth in several rock types. To re-parameterize the Argento et al. (2015b) results in a form conducive to use in Eq. (3), we fit exponential functions to the polynomials for ^{36}Cl from K and ^{10}Be in quartz production with depth in granite. However, because the attenuation length for the fit to the ^{10}Be in quartz polynomial is lower (141 g cm^{-2}) than the conventional value for the ^{10}Be in quartz attenuation length in rock (ca. 160 g cm^{-2}), rather than using the best-fit ^{36}Cl attenuation length directly, we multiply the modeled $^{36}Cl_K/^{10}Be_{qtz}$ attenuation length ratio (ca. 1.1) by 160 g cm^{-2} to estimate the attenuation length for ^{36}Cl from K production in rock. Although this approach does not capture the precise shape of the modeled ^{36}Cl from the K production profile, the accuracy is likely sufficient when considering only depth-integrated production under steady-state erosion.

To model subsurface attenuation for ^{36}Cl production from Fe, which has too high of a threshold energy to be affected by increases in nucleon multiplicity in the subsurface, we use the atmospheric production model described in Sect. 2.1. This approach assumes that the evolution of the cosmic-ray energy spectrum with depth in the subsurface, above the relevant threshold energies, is similar to that in the atmosphere. Production profiles for ^{36}Cl from Fe and ^{10}Be in quartz were generated between the elevation of Mount Evans (4300 m) and sea level, equivalent to ca. 410 g cm^{-2} of mass depth (the model is not valid below sea level), and exponential functions were fit to each. Attenuation lengths for all reactions are longer in the subsurface than in the atmosphere because the average atomic mass in rock is greater than in air. Thus, the modeled attenuation lengths in the atmosphere must be adjusted upwards. To do this, the modeled $^{36}Cl_{Fe}/^{10}Be_{qtz}$ attenuation length ratio in the atmosphere (ca. 0.9) is multiplied by 160 g cm^{-2} to obtain the ^{36}Cl from Fe subsurface attenuation length.

This approach gives unique attenuation lengths for each of the three relevant spallation reactions in the sample from Mount Evans ($^{36}Cl_K$ = 176 g cm^{-2}, $^{36}Cl_{Fe}$ = 146 g cm^{-2}, and $^{10}Be_{qtz}$ = 160 g cm^{-2}). Production of ^{36}Cl from Fe thus declines more rapidly with increasing mass depth in the subsurface than ^{10}Be in quartz and much more rapidly than ^{36}Cl from K. This implies that, when considering only spallation, a sample experiencing steady-state erosion at high elevation should have a $^{36}Cl_{Fe}/^{36}Cl_K$ concentration ratio that differs by ca. 20 % from the ratio expected under constant exposure and no erosion.

2.4.3 Low-energy neutrons

Production of ^{36}Cl by low-energy neutron capture by ^{35}Cl is strongly influenced by snow cover and pore water because of the neutron scattering and absorbing properties of H. Modest snow cover increases the neutron flux just below the air–ground interface by preventing diffusive neutron leakage into the atmosphere (Zweck et al., 2013). Likewise, the presence of up to ca. 4 wt % water in soil pores increases thermal neutron fluxes by enhancing thermalization in the subsurface, although larger amounts of pore water decrease fluxes by enhancing neutron absorption (Phillips et al., 2001). The Owens Valley samples are clasts that were embedded in the surface of a moraine and are subject to the effects of both snow shielding and pore water in the adjacent morainal sediment. However, because low-energy neutron fluxes do not affect the accumulation of ^{10}Be in quartz, and because the production rate of ^{36}Cl from K is known, the K-feldspar–quartz pair can be used to estimate sample-specific neutron capture production rates. We use these adjusted values for our production rate and ratio calibrations for the Owens Valley site. A similar calculation is not necessary at Mount Evans because of the low chloride concentrations.

2.4.4 Scaling factor ratios

To examine changes in $^{36}Cl_{Fe}/^{10}Be_{qtz}$ and $^{36}Cl_{Fe}/^{36}Cl_K$ with altitude, the calibrated production rates at the study sites are first normalized by the production rate of either ^{10}Be in quartz or ^{36}Cl from K at the samples' locations, whichever the calibration was conducted against, thus giving production ratios. To normalize differences in geomagnetic scaling between the sites, the production rates at the calibration sites are then divided by the production ratios at sea level at their geographic locations. In this normalization scheme, all scaling factors are calculated using the reaction-specific scaling model of Lifton et al. (2014). Reference SLHL production rates are taken from Marrero et al. (2016) for ^{10}Be in quartz and ^{36}Cl from K. The SLHL production rate of Fe is taken from the inverse-error-weighted average SLHL production rate of the calibration samples (Table 2), excluding OV19-1 as an outlier (Sect. 3.2). The total normalization can be expressed as

$$R_{Fe/K,Be} = \left(\frac{P_{Fe,cal}}{S_{K,Be}\times P_{K,Be,SLHL}}\right) \Big/ \left(\frac{S_{Fe,0}\times P_{Fe,SLHL}}{S_{K,Be,0}\times P_{K,Be,SLHL}}\right) = \left(\frac{P_{Fe,cal}}{S_{K,Be}}\right) \Big/ \left(\frac{S_{Fe,0}\times P_{Fe,SLHL}}{S_{K,Be,0}}\right), \quad (4)$$

where $R_{Fe/K,Be}$ is the resulting altitude scaling factor ratio, $P_{Fe,cal}$ is the production rate of ^{36}Cl from Fe at the calibration site (as calculated from the data, using the approach outlined in Sect. 2.4.1), $S_{K,Be}$ is the scaling factor for production of ^{36}Cl from K or ^{10}Be in quartz from SLHL to the site, $S_{K,Be,0}$ is the scaling factor for production of ^{36}Cl from K or ^{10}Be in quartz from SLHL to sea level at the site, and $S_{Fe,0}$ is the scaling factor for ^{36}Cl production from Fe from SLHL to sea level at the site. Finally, $P_{Fe,SLHL}$ is the production rate of ^{36}Cl from Fe at SLHL, which is determined from the average of all calibration data. The SLHL production rate of $^{36}Cl_K$ or $^{10}Be_{qtz}$ ($P_{K,Be,SLHL}$) is in both the numerator and denominator and thus cancels out. This approach allows us to examine whether deviations in production ratios from the average ratio are consistent with the modeled scaling behavior by comparing calibrated scaling factor ratios with model predictions using statistical hypothesis testing and goodness-of-fit metrics.

3 Results

3.1 Modeling results

The modeled changes in $^{36}Cl_{Fe}/^{10}Be_{qtz}$ and $^{36}Cl_{Fe}/^{36}Cl_K$ production ratios with altitude are shown in Fig. 3. The model predicts that the scaling of ^{36}Cl production from Fe departs significantly from lower-energy reactions, increasing by approximately 40 % from sea level to 5.5 km (ca. 500 hPa) relative to ^{10}Be in quartz and by slightly more relative to ^{36}Cl from K, which is sensitive to even lower energies (Fig. 1). At the study sites, the model predicts an increase in the $^{36}Cl_{Fe}/^{10}Be_{qtz}$ production ratio of 18 % and in the $^{36}Cl_{Fe}/^{36}Cl_K$ production ratio of 22 % between Owens Valley and Mount Evans. Next, we test these predictions against empirical data.

3.2 Measurement results and scaling factor ratios

Measured ^{36}Cl concentrations in magnetite and K-feldspar, ^{10}Be concentrations in quartz, and target and bulk-rock chemistries are presented in the Supplement. All measured nuclide concentrations are corrected by procedural blanks, which account for less than 5 % of the ^{36}Cl and 2 % of the ^{10}Be inventory in any sample. Stable Cl inventories are corrected by blanks ranging from 73 to 100 µg of Cl. For the Mount Evans magnetite sample, the blank correction produces a negative Cl concentration, so the Mount Evans magnetite is assumed to have no stable Cl. Magnetite target chemistry is dominated by Fe, although neutron capture on Cl is also a significant production pathway in the Owens Valley samples. Spallation from K is the largest source of ^{36}Cl in all feldspar samples, while low-energy neutron capture is the second most important pathway (except in OV19-3, in which the two are subequal) (see the Table labeled "Computed parameters" in the Supplement). The radiogenic ^{36}Cl inventory is computed by assuming secular equilibrium between radiogenic production and decay (Marrero et al., 2016) and subtracted from the reported concentrations. These corrected concentrations are then used to calibrate production rates. Analysis of the effects of environmental water on the low-energy neutron fluxes from the K-feldspar–quartz pair at Owens Valley (Sect. 2.4.3) indicates that neutron capture production rates are 19 %–36 % higher than in the absence of pore water and snow cover. These elevated neutron capture production rates are used in the calibration. Calibrated production rates are shown in Table 2.

Calibrated scaling factor ratios for the Owens Valley samples range from 0.47 ± 0.10 to 1.15 ± 0.08, with inverse-error-weighted means of 0.96 ± 0.05 for $^{36}Cl_{Fe}/^{36}Cl_K$ and 0.97 ± 0.05 for $^{36}Cl_{Fe}/^{10}Be_{qtz}$. In both cases, OV19-1 produces a scaling factor ratio that is >3σ lower than the mean, which may be because of an overestimate of the stable Cl concentration in the magnetite and consequently of the importance of neutron capture. The blank correction accounts for more than 50 % of the total Cl in this sample, suggesting that variability in the amount of Cl introduced during sample preparation between the blank and the sample may significantly impact the total Cl inventory. Therefore, we exclude this sample as an outlier and recalculate the mean values as 1.13 ± 0.06 and 1.12 ± 0.05 for the $^{36}Cl_K$ and $^{10}Be_{qtz}$ normalized ratios, respectively. At Mount Evans, the calibrated scaling factor ratios are 1.38 ± 0.10 for $^{36}Cl_{Fe}/^{36}Cl_K$ and 1.29 ± 0.09 for $^{36}Cl_{Fe}/^{10}Be_{qtz}$. Ratios generally increase with altitude (Fig. 5).

3.3 Model evaluation

To evaluate the altitude scaling of $^{36}Cl_{Fe}$ production, we compare modeled scaling factor ratios to the calibrated values. First, we examine the null hypothesis that ratios at Mount Evans (ca. 4300 m) and Owens Valley (ca. 1700 m) are identical. For the $^{36}Cl_{Fe}/^{36}Cl_K$ ratio, the z statistic is 2.23 and for the $^{36}Cl_{Fe}/^{10}Be_{qtz}$ ratio the z-statistic is 1.64, indicating probabilities of 0.01 and 0.05 for the null hypothesis and that therefore the high- and low-elevation sites are statistically distinguishable at greater than the 90 % confidence level.

Next, we use the chi-squared goodness-of-fit test to evaluate how well the reaction-specific model fits the calibration data. The chi-squared statistic measures the difference between modeled and observed values, where a lower value of the statistic implies a tighter fit of the model to the observations (Bevington and Robinson, 1992). We also report p values for the hypothesis that the model describes the data and the chi-squared statistic normalized by the number of degrees of freedom (i.e., the reduced chi-squared statistic or the mean square of the weighted deviates, MSWD). To compare only independent data, we calculate statistics for the $^{36}Cl_K$ and $^{10}Be_{qtz}$ normalized ratios independently. The reaction-specific model fits the mean $^{36}Cl_{Fe}/^{36}Cl_K$ ratios with a chi-squared statistic of 0.021 with 1 degree of freedom (MSWD = 0.021, p = 0.89) and the $^{36}Cl_{Fe}/^{10}Be_{qtz}$ ratios with a chi-squared statistic of 0.249 (2 degrees of freedom, MSWD = 0.125, p = 0.88). Conversely, an integral flux scaling model that uses the same scaling factors for all reactions (i.e., a horizontal line in Fig. 5) fits the $^{36}Cl_{Fe}/^{36}Cl_K$ production ratio with a chi-squared statistic of 4.97 (1 degree of freedom, MSWD = 4.97, p = 0.03) and the $^{36}Cl_{Fe}/^{10}Be_{qtz}$ ratios with a chi-squared statistic of 3.37 (2 degrees of freedom, MSWD = 1.69, p = 0.19). Thus, the uniform scaling factor model can be rejected at an α value of 0.1 for $^{36}Cl_{Fe}/^{36}Cl_K$ but cannot be rejected at this level for $^{36}Cl_{Fe}/^{10}Be_{qtz}$. However, in both cases, the reaction-specific scaling model fits the data more closely than the integral flux model. This may indicate that the uncertainties in the empirical ratios are overestimated.

4 Discussion

4.1 Implications

These results imply that ^{36}Cl production from Fe can be more accurately scaled using reaction-specific scaling factors than integral-flux scaling factors. This is significant for assessing ^{36}Cl production rates in Fe-oxide minerals, such as magnetite, which is a promising target mineral for determining catchment-averaged erosion rates on mafic rocks (Moore and Granger, 2019b). When normalized to ^{10}Be in quartz, the reaction-specific scaling model using the new calibration data produces an inverse-error-weighted SLHL reference production rate of 1.35 ± 0.06 atoms g^{-1} Fe yr^{-1} and 1.31 ± 0.07 atoms g^{-1} Fe yr^{-1} when normalized to ^{36}Cl in K-feldspar. Both reference production rates are within 2σ error of the estimate of 1.28 ± 0.03 atoms g^{-1} Fe yr^{-1} made by Moore and Granger (2019a).

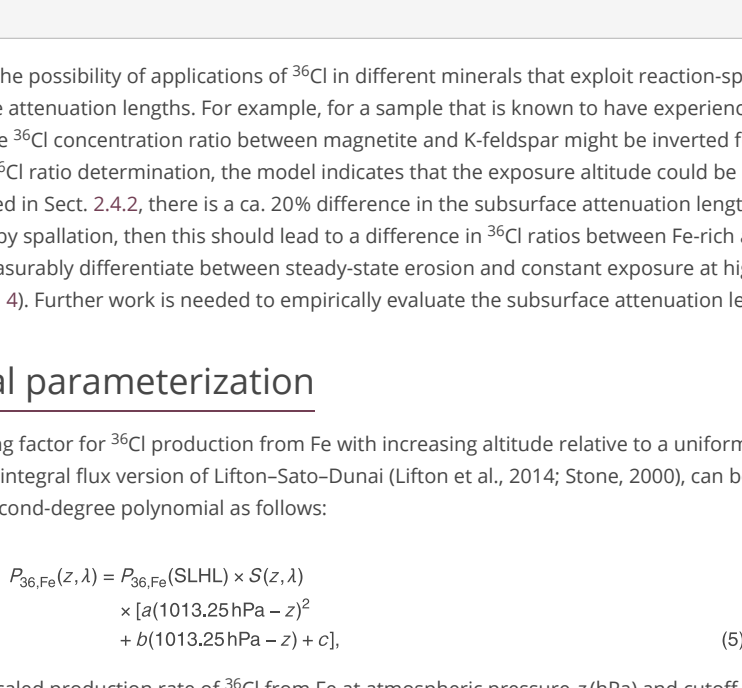

Figure 5 Model–data comparison. Modeled production ratio deviation from sea level for $^{36}Cl_K/^{10}Be_{qtz}$ (blue) and $^{36}Cl_{Fe}/^{36}Cl_K$ (orange). Data points show measured $^{36}Cl_{Fe}/^{36}Cl_K$ and $^{36}Cl_{Fe}/^{10}Be_{qtz}$ scaling factor ratios at the three calibration sites (OV19-1 has been omitted as an outlier). Site means are shown by blue- and orange-colored symbols and are offset in the y direction to avoid an error bar overlap. Error bars are 1σ. Measured production ratios show a general trend of increasing with decreasing air pressure. The ratios at the low- and high-elevation sites are distinguishable from each other for both reaction pairs at greater than the 90 % confidence interval. The dashed black line shows the second-degree polynomial fit to the modeled $^{36}Cl_{Fe}/^{10}Be_{qtz}$ ratios.

Download

This work also suggests the possibility of applications of ^{36}Cl in different minerals that exploit reaction-specific scaling or differences in subsurface attenuation lengths. For example, for a sample that is known to have experienced steady-state erosion or constant exposure, the ^{36}Cl concentration ratio between magnetite and K-feldspar might be inverted for the exposure altitude. Given a 5 % error in the ^{36}Cl ratio determination, the model indicates that the exposure altitude could be resolved to ca. ±600 m (1σ). Likewise, if, as argued in Sect. 2.4.2, there is a ca. 20 % difference in the subsurface attenuation length between production of ^{36}Cl from Fe and from K by spallation, then this should lead to a difference in ^{36}Cl ratios between Fe-rich and K-rich mineral separates that could measurably differentiate between steady-state erosion and constant exposure at high-erosion rates and short exposure ages (Fig. 4). Further work is needed to empirically evaluate the subsurface attenuation lengths of these reactions.

4.2 Polynomial parameterization

The increase in the scaling factor for ^{36}Cl production from Fe with increasing altitude relative to a uniform scaling factor model, such as Lal–Stone or the integral flux version of Lifton–Sato–Dunai (Lifton et al., 2014; Stone, 2000), can be reasonably approximated using a second-degree polynomial as follows:

$$P_{36,Fe}(z,\lambda) = P_{36,Fe}(\mathrm{SLHL}) \times S(z,\lambda) \times [a(1013.25\,\mathrm{hPa} - z)^2 + b(1013.25\,\mathrm{hPa} - z) + c], \quad (5)$$

where $P_{36,Fe}(z,\lambda)$ is the scaled production rate of ^{36}Cl from Fe at atmospheric pressure z (hPa) and cutoff rigidity λ (GV); $P_{36,Fe}$(SLHL) is the reference production rate of ^{36}Cl from Fe at SLHL; $S(z,\lambda)$ is the scaling factor from an integral flux scaling model; and a, b, and c are polynomial coefficients. This formulation allows a straightforward modification of integral flux scaling factors that are commonly used to scale ^{10}Be production to accommodate ^{36}Cl scaling from Fe that captures the shape of the curve in Fig. 5 with good fidelity between sea level (1013 hPa) and ca. 5.5 km (500 hPa). Best-fit polynomial coefficients calculated at 1 GV intervals between 0 and 14 GV are presented in the Supplement, although the shape of the curve is only weakly sensitive to the cutoff rigidity.

5 Conclusions

Modeling using excitation functions and cosmic-ray nucleon fluxes predicts that ^{36}Cl production from Fe attenuates more rapidly in the atmosphere than reactions that are sensitive to lower energies. The $^{36}Cl_{Fe}/^{36}Cl_K$ production ratio is predicted to increase with elevation at an average rate of approximately 0.84 % per 100 m between sea level and the elevation of the Mount Evans sample (4300 m a.s.l.) and by slightly less when normalized to ^{10}Be in quartz. We evaluated this prediction against measured scaling factor ratios between ^{36}Cl in magnetite and ^{36}Cl in K-feldspar and ^{10}Be in quartz across an altitude transect. Samples with late-glacial exposure histories at elevations of ca. 1700 and 4300 m a.s.l. in western North America produce scaling factor ratios that differ at greater than the 90 % confidence level and that fit a reaction-specific scaling model more closely than a uniform flux scaling model. Thus, reaction-specific scaling factors are likely appropriate for the scaling production of ^{36}Cl from Fe, especially when analyzing ^{36}Cl in magnetite and other Fe-rich materials where spallation from Fe is the dominant production pathway.

Code and data availability

All new research data are provided in the Supplement. The codes used to calibrate the production rates are available at https://github.com/magnesiowustite/Altitude-scaling-of-Cl-36-production-from-Fe (last access: 13 October 2024; DOI: https://doi.org/10.5281/zenodo.13925210, Moore, 2024).

Supplement

The supplement related to this article is available online at: https://doi.org/10.5194/gchron-6-541-2024-supplement.

Author contributions

AKM conceptualized the study and conducted the investigation and formal analysis. AKM and DEG acquired funding, and DEG provided laboratory resources. AKM wrote the paper with input from DEG.

Competing interests

The contact author has declared that neither of the authors has any competing interests.

Disclaimer

Publisher's note: Copernicus Publications remains neutral with regard to jurisdictional claims made in the text, published maps, institutional affiliations, or any other geographical representation in this paper. While Copernicus Publications makes every effort to include appropriate place names, the final responsibility lies with the authors.

Acknowledgements

We would like to thank Will Odom and Zach Meyers for collecting the Owens Valley samples, the PRIME Lab staff for AMS measurements, and Christopher Halsted and Irene Schimmelpfennig for reviews that helped improve this work. We thank Greg Balco for editorial handling.

Financial support

This research has been supported by the Directorate for Geosciences (grant no. EAR-2011342).

Review statement

This paper was edited by Greg Balco and reviewed by Christopher Halsted and Irene Schimmelpfennig.

References

Amidon, W. H., Farley, K. A., Burbank, D. W., and Pratt-Sitaula, B.: Anomalous cosmogenic ^{3}He production and elevation scaling in the high Himalaya, Earth Planet. Sc. Lett., 265, 287–301, https://doi.org/10.1016/j.epsl.2007.10.022, 2008.

Argento, D. C., Reedy, R. C., and Stone, J. O.: Modeling the earth's cosmic radiation, Nucl. Instrum. Meth. B, 294, 464–469, https://doi.org/10.1016/j.nimb.2012.05.022, 2013.

Argento, D. C., Stone, J. O., Reedy, R. C., and O'Brien, K.: Physics-based modeling of cosmogenic nuclides part I – Radiation transport methods and new insights, The CRONUS-EARTH Volume: Part I, Quat. Geochronol., 26, 29–43. https://doi.org/10.1016/j.quageo.2014.09.004, 2015a.

Argento, D. C., Stone, J. O., Reedy, R. C., and O'Brien, K.: Physics-based modeling of cosmogenic nuclides part II – Key aspects of in-situ cosmogenic nuclide production, The CRONUS-EARTH Volume: Part I, Quat. Geochronol., 26, 44–55, https://doi.org/10.1016/j.quageo.2014.09.005, 2015b.

Balco, G.: Production rate calculations for cosmic-ray-muon-produced ^{10}Be and ^{26}Al benchmarked against geological calibration data, Quat. Geochronol., 39, 150–173, https://doi.org/10.1016/j.quageo.2017.02.001, 2017.

Bevington, P. R. and Robinson, D. K.: Data reduction and error analysis for the physical sciences, WCB McGraw-Hill, New York, ISBN 9780079112439/0079112439, 1992.

Blanckenburg, F. von and Willenbring, J. K.: Cosmogenic Nuclides: Dates and Rates of Earth-Surface Change, Elements, 10, 341–346, https://doi.org/10.2113/gselements.10.5.341, 2014.

Blard, P.-H., Braucher, R., Lavé, J., and Bourlès, D.: Cosmogenic ^{10}Be production rate calibrated against ^{3}He in the high Tropical Andes (3800–4900m, 20–22°S), Earth Planet. Sc. Lett., 382, 140–149, https://doi.org/10.1016/j.epsl.2013.09.010, 2013.

Corbett, L. B., Bierman, P. R., Rood, D. H., Caffee, M. W., Lifton, N. A., and Woodruff, T. E.: Cosmogenic ^{26}Al/^{10}Be surface production ratio in Greenland, Geophys. Res. Lett., 44, 1350–1359, 2017.

Gayer, E., Pik, R., Lavé, J., France-Lanord, C., Bourlès, D., and Marty, B.: Cosmogenic ^{3}He in Himalayan garnets indicating an altitude dependence of the ^{3}He/^{10}Be production ratio, Earth Planet. Sc. Lett., 229, 91–104. https://doi.org/10.1016/j.epsl.2004.10.009, 2004.

Granger, D. E., Lifton, N. A., and Willenbring, J. K.: A cosmic trip: 25 years of cosmogenic nuclides in geology, Geol. Soc. Am. Bull., 125, 1379–1402, https://doi.org/10.1130/B30774.1, 2013.

Halsted, C. T., Bierman, P. R., and Balco, G.: Empirical Evidence for Latitude and Altitude Variation of the In Situ Cosmogenic ^{26}Al/^{10}Be Production Ratio, Geosciences, 11, 402, https://doi.org/10.3390/geosciences11100402, 2021.

Lal, D. and Peters, B.: Cosmic Ray Produced Radioactivity on the Earth, in: Kosmische Strahlung II/Cosmic Rays II, Handbuch der Physik/Encyclopedia of Physics, edited by; Sitte, K., Springer Berlin Heidelberg, https://doi.org/10.1007/978-3-642-46079-1_7, pp. 551–612, 1967.

Leontaritis, A. D., Pavlopoulos, K., Marrero, S. M., Ribolini, A., Hughes, P. D., and Spagnolo, M.: Glaciations on ophiolite terrain in the North Pindus Mountains, Greece: New geomorphological insights and preliminary ^{36}Cl exposure dating, Geomorphology, 413, 108335, https://doi.org/10.1016/j.geomorph.2022.108335, 2022.

Lifton, N., Sato, T., and Dunai, T. J.: Scaling in situ cosmogenic nuclide production rates using analytical approximations to atmospheric cosmic-ray fluxes, Earth Planet. Sc. Lett., 386, 149–160, 2014.

Marrero, S. M., Phillips, F. M., Borchers, B., Lifton, N., Aumer, R., and Balco, G.: Cosmogenic nuclide systematics and the CRONUScalc program, Quat. Geochronol., 31, 160–187, 2016.

Masarik, J. and Beer, J.: An updated simulation of particle fluxes and cosmogenic nuclide production in the Earth's atmosphere, J. Geophys. Res., 114, D11103, https://doi.org/10.1029/2008JD010557, 2009.

Moore, A.: magnesiowustite/Altitude-scaling-of-Cl-36-production-from-Fe: Scaling Codes (1.0), Zenodo [code and data set], https://doi.org/10.5281/zenodo.13925210, 2024.

Moore, A. K. and Granger, D. E.: Calibration of the production rate of cosmogenic ^{36}Cl from Fe, Quat. Geochronol., 51, 87–98, https://doi.org/10.1016/j.quageo.2019.02.002, 2019a.

Moore, A. K. and Granger, D. E.: Watershed-averaged denudation rates from cosmogenic ^{36}Cl in detrital magnetite, Earth Planet. Sc. Lett., 527, 115761, https://doi.org/10.1016/j.epsl.2019.115761, 2019b.

Moore, A. K., Méndez Méndez, K., Hughes, K. S., and Granger, D. E.: Volcanic Arc Weathering Rates in the Humid Tropics Controlled by the Interplay Between Physical Erosion and Precipitation, AGU Advances, 5, e2023AV001066, https://doi.org/10.1029/2023AV001066, 2024.

Nishiizumi, K., Winterer, E. L., Kohl, C. P., Klein, J., Middleton, R., Lal, D., and Arnold, J. R.: Cosmic ray production rates of ^{10}Be and ^{26}Al in quartz from glacially polished rocks, J. Geophys. Res., 94, 17907–17915, https://doi.org/10.1029/JB094iB12p17907, 1989.

Nishiizumi, K., Imamura, M., Caffee, M. W., Southon, J. R., Finkel, R. C., and McAninch, J.: Absolute calibration of ^{10}Be AMS standards, Nucl. Instrum. Meth. B, 258, 403–413, https://doi.org/10.1016/j.nimb.2007.01.297, 2007.

Phillips, F. M.: Cosmogenic nuclide data sets from the Sierra Nevada, California, for assessment of nuclide production models: I. Late Pleistocene glacial chronology, Quat. Geochronol., 35, 119–129, https://doi.org/10.1016/j.quageo.2015.12.003, 2016.

Phillips, F. M., Stone, W. D., and Fabryka-Martin, J. T.: An improved approach to calculating low-energy cosmic-ray neutron fluxes near the land/atmosphere interface, Chem. Geol., 175, 689–701, https://doi.org/10.1016/S0009-2541(00)00329-6, 2001.

Phillips, F. M., Zreda, M., Plummer, M. A., Elmore, D., and Clark, D. H.: Glacial geology and chronology of Bishop Creek and vicinity, eastern Sierra Nevada, California, Geol. Soc. Am. Bull., 121, 1013–1033, https://doi.org/10.1130/B26271.1, 2009.

Reedy, R. C.: Cosmogenic-nuclide production rates: Reaction cross section update, Proceedings of the Twelfth International Conference on Accelerator Mass Spectrometry, Wellington, New Zealand, 20–25 March 2011, Nucl. Instrum. Meth. B,, 294, 470–474, https://doi.org/10.1016/j.nimb.2011.08.034, 2013.

Sato, T., Yasuda, H., Niita, K., Endo, A., and Sihver, L.: Development of PARMA: PHITS-based Analytical Radiation Model in the Atmosphere, Radiat. Res., 170, 244–259, https://doi.org/10.1667/RR1094.1, 2008.

Schiekel, T., Sudbrock, F., Herpers, U., Gloris, M., Leya, I., Michel, R., Synal, H.-A., and Suter, M.: On the production of ^{36}Cl by high energy protons in thin and thick targets, Nucl. Instrum. Meth. B, 113, 484–489, 1996.

Schimmelpfennig, I., Williams, A., Pik, R., Burnard, P., Niedermann, S., Finkel, R., Schneider, B., and Benedetti, L.: Inter-comparison of cosmogenic in-situ ^{3}He, ^{21}Ne and ^{36}Cl at low latitude along an altitude transect on the SE slope of Kilimanjaro volcano (3°S, Tanzania), Quat. Geochronol., 6, 425–436, https://doi.org/10.1016/j.quageo.2011.05.002, 2011.

Sharma, P., Kubik, P. W., Fehn, U., Gove, H. E., Nishiizumi, K., and Elmore, D.: Development of ^{36}Cl standards for AMS, Nucl. Instrum. Meth. B, 52, 410–415, https://doi.org/10.1016/0168-583X(90)90447-3, 1990.

Stone, J. O., Air pressure and cosmogenic isotope production, J. Geophys. Res., 105, 23753–23759, https://doi.org/10.1029/2000JB900181, 2000.

Uppala, S. M., KÅllberg, P. W., Simmons, A. J., Andrae, U., Bechtold, V. D. C., Fiorino, M., Gibson, J. K., Haseler, J., Hernandez, A., Kelly, G. A., Li, X., Onogi, K., Saarinen, S., Sokka, N., Allan, R. P., Andersson, E., Arpe, K., Balmaseda, M. A., Beljaars, A. C. M., Berg, L. V. D., Bidlot, J., Bormann, N., Caires, S., Chevallier, F., Dethof, A., Dragosavac, M., Fisher, M., Fuentes, M., Hagemann, S., Hólm, E., Hoskins, B.J., Isaksen, L., Janssen, P. A. E. M., Jenne, R., Mcnally, A. P., Mahfouf, J.-F., Morcrette, J.-J., Rayner, N. A., Saunders, R. W., Simon, P., Sterl, A., Trenberth, K. E., Untch, A., Vasiljevic, D., Viterbo, P., Woollen, J.: The ERA-40 re-analysis, Q. J. Roy. Meteor. Soc., 131, 2961–3012, https://doi.org/10.1256/qj.04.176, 2005.

Zweck, C., Zreda, M., and Desilets, D.: Snow shielding factors for cosmogenic nuclide dating inferred from Monte Carlo neutron transport simulation, Earth Planet. Sc. Lett., 379, 64–71, 2013.